An Early-Mid Holocene process of regional desertification recorded in aeolian sediments from the northern slope of the middle Himalayan Mountains

Yang Gao[1, 2], Keqi Zhang[1, 3], Zhonghai Wu[1, 3], Tingting Tian[1, 3], Hailong Gai[4], Jiameng Zuo[1], Bin Li[1]

[1]Institute of Geomechanics, Chinese Academy of Geological Sciences, Beijing, 100081, China
[2]School of Earth and Space Sciences, Peking University, Beijing, 100871, China
[3]Key Laboratory of Active Tectonics and Geological Safety, Ministry of Natural Resources, Beijing, 100081, China
[4]Qinghai Earthquake Agency, Xining, 810001, China

Correspondence to: Keqi Zhang (zhkeqi@163.com) and Zhonghai Wu (wuzhonghai8848@foxmail.com)

Abstract. Aeolian sediments, a sensitive paleoclimatic and paleoenvironmental archive, are widely distributed over the Tibetan Plateau. In the northern slope of the Himalayan Mountains, however, the potential linkages between the aeolian processes, climatic changes, and the processes of desertification during the Holocene are not well understood. Here, we use an aeolian record from the northern slope of the middle Himalayan Mountains to investigate the influences of paleoclimate and paleoenvironment during the Early-Mid Holocene through the optically stimulated luminescence (OSL) dating, magnetic parameters, color variations, scanning electron microscope (SEM) and energy dispersive spectrometer (EDS), and grain size parameters. Glacial sediments, weathering products, the surface of lack of vegetation cover, and alluvium and ancient lacustrine sediments had provided the sources for the aeolian sediments. The strengthened Indian monsoon intensity, dry and warm climate, and sparse vegetation cover accelerated the rapid expansion of desertification between ~11 and 9.6 ka B.P.. The Indian monsoon intensity weakened between 9.6 and 6.3 ka B.P., the warm and humid climate and increased vegetation cover decelerated the rapid expansion of desertification. Influenced by the weakened Indian monsoon intensity, warm and humid climate, increased vegetation cover, and limited sources, the desertification decelerated further between 6.3 and ~4.5 ka B.P.. Further, the linkage and interplay between changes in the Indian monsoon, vegetation cover, sources, and landforms play a key role in aeolian processes and regional processes of desertification in the northern slope Himalayan Mountains during the Early-Mid Holocene.

1 Introduction

The Himalayan Mountains, known as a barrier between the Tibetan Plateau to the north and the Indian continent to the south, play a significant role in the climate and ecological systems of the Tibetan Plateau, and South and East Asia (Ye and Wu, 1998; Molnar et al., 1993; 2010; An et al., 2001; Owen, et al., 2002; Immerzeel et al., 2010; Wu et al., 2012). A large amount of precipitation and rich vegetation cover are produced on the southern slope of the Himalayan Mountains because the high elevation topography provides orographic obstruction to moving northward moist marine air of the Indian monsoon

(Gadgil, 2003; Lekshmy et al.,2014; Wicander, and Monroe, 2017). As a result, desertification is widespread on the northern slope of the Himalayan Mountains and most parts of the Tibetan Plateau (Cui et al., 2009; Xian et al., 2009; Zhang et al., 2012; Lu et al., 2015; Li et al., 2019). Therefore, studies of climatic and environmental changes over the northern slope of the Himalayan Mountains which is bordered on the north by the Tibetan Plateau are important to understand the changes of

35   climate and environment in Tibetan Plateau and South and East Asia, as well as to ameliorate the regional ecological environment.

During the Holocene, it has been suggested that the Indian monsoon has controlled the southern Tibetan Plateau (An et al., 2012; Zhu et al., 2015). The modern precipitation δ18O observations and simulations also showed that the southern Tibetan Plateau is dominated by the Indian monsoon (Yao et al., 2013). Several continuous paleoclimate data over the southern

40   Tibetan Plateau are mainly derived from speleothem records (Cai et al., 2012), lacustrine sedimentary records (Wang et., 2002; Henderson et al., 2013; Rades et al., 2013; Günther et al., 2015; Wünnemann et al., 2015; Alivernini et al., 2018), and pollen records (Huang, 2000; Lu et al., 2011; Tang et al., 2021). In general, these records are used to reconstruct the changes of the Indian monsoon and the Holocene climate changes, and these reconstructed results of climate changes are roughly similar during the Holocene, generally indicating several regional humid and dry intervals. Beyond these records, the records

45   from aeolian sediments are also used to reconstruct the Holocene climatic and environmental changes in the southern Tibetan Plateau (Li et al., 1999; Kaiser et al., 2009; Lai et al., 2009; Pan et al., 2014; Li et al., 2016; Ling et al., 2020; Huang et al., 2022). The majority of these aeolian sediments developed at low altitudes of the southern Tibetan Plateau. Moreover, the distribution of aeolian sediments is closely related to the geomorphological units, such as flood plains and river terraces, lakeshores, dry basins, and mountain slopes (Dong et al., 2017). However, the potential linkages between the aeolian

50   processes, climatic changes, and environmental changes (e.g., the processes of desertification) during the Holocene at high altitudes of the southern Tibetan Plateau are not well understood, especially for the northern slope of the Himalayan Mountains because it is sensitive to the desertification.

In this study, we reconstruct the Early-Mid Holocene process of regional desertification through the magnetic properties, color variations, grain size characteristics, and sedimentary characteristics of sand grains of aeolian sediments from profile

55   Pala, the northern slope of the middle Himalayan Mountains based on the optically stimulated luminescence (OSL) dating. Our study aims to analyze the sources of aeolian sediments, change in Indian monsoon intensity inferred from aeolian sediments proxy, and the linkages between climate changes, aeolian activity, and process of desertification. Furthermore, we also discuss the implications of aeolian sediments in the northern slope of the middle Himalayan Mountains for the paleoclimate and paleoenvironment.

60   **2 Regional setting**

The Pala (28°18′57″ N, 87°25′26″ E) lies at 4325 m above sea level on the northern slope of the Himalayan mountains, southern Tibetan Plateau. It is close to Pum Qu and belongs to the town of Guojia, Dinggye County, Xigaze (Fig. 1 a).

Moreover, glacial sediments are widespread on the surrounding area of Pala and even the northern slope of the Himalayan mountains. The aeolian sediments distribute on the upland and near the glacial sediments (Fig. 1 c). By combining the field

65   investigations with satellite data, the surface area (about 1.5 km ^{2}) of aeolian sediments in Pala was measured. The grain size of sands in the sediments is less than 0.5 mm according to the preliminary field observations. Any sedimentary beddings were not found in the aeolian sands of this profile.

The Pala is located on the southern segment of the north-south trending Xaiza-Dinggye rift (XDR) (Armijo et al., 1986; Zhang et al., 2002; Zhang and Guo, 2007). Next to the XDR is Pum Qu, a river that breaks the lofty middle Himalayan

70   Mountains barrier and flows south into Gangetic Plains. A near north-south trending deep gorges that have been carved by the Pum Qu connect the northern slope of the middle Himalayan Mountains and Gangetic Plains (GP). Such gorges provide channels for the inflow of moisture-laden warm winds from the south (Dhital, 2015). In addition, the major rock types around the Pala, forming the major sources of detritus for the aeolian sediments, consist of Meso-and Neoproterozoic Zhaxirega Formation-complex (mainly composed of gneiss, granulite, migmatite, and migmatitic gneiss), Ordovician

75   (dominated by limestone), Devonian and Carboniferous (dominated by limestone and sandstone), Triassic (dominated by limestone and sandstone), Quaternary (composed of alluvial deposit (Q_4), proluvium (Q_4), glacial till (Q_3), lacustrine deposit (Q_{2-3}),) monzogranite, and gneiss (Li, 2001b) (Fig. 1 b). Furthermore, the Zhaxirega Formation-complex covers most of the area around the Pala.

3 Methods

3.1 Field methods

80   In the study area and nearby area, both aeolian sands and glacial drifts were deposited when we investigated during the summer of 2020. In this study, four samples for OSL dating, five representative samples for scanning electron microscope and energy dispersive spectrometer (SEM-EDS), and a total of 82 samples for rock magnetism, frequency magnetic susceptibility, grain size analysis, and color variations analysis were taken from the profile Pala about 3 m thick (Fig. 1 c and

85   Fig. 2 a). To achieve a high data resolution, a maximum vertical interval of 4 cm for 87 samples was carried out.

3.2 Laboratory methods

Total four OSL dating samples were drilled respectively from the depth of 30cm, 80cm, 160cm, and 260 cm using stainless steel tubes of about 5 cm diameter and 25 cm length hammered into the vertical surface of cleaned sediments. The tubes which were filled with sediments were wrapped up in black lightproof plastic bags and tinfoil.

90   OSL (blue light LEDs, λ=880 nm) of the quartz grain size 4-11 μm and 90-125 μm was carried out in the Key Laboratory of Active Tectonics and Geological Safety, Ministry of Natural Resources at the Institute of Geomechanics, Chinese Academy of Geological Sciences using a Daybreak 2200 OSL reader in this study.

High-frequency magnetic susceptibility (χ_{hf}) and low-frequency magnetic susceptibility (χ_{lf}) were measured under 4.65 kHz and 0.465 kHz magnetic field in the Key Laboratory of Active Tectonics and Geological Safety, Ministry of Natural

95 Resources at the Institute of Geomechanics, Chinese Academy of Geological Sciences using a Bartinton-MS2 meter. Percentage frequency-dependent magnetic susceptibility (χ_{fd}) is calculated here as equation (1) (Liu et al., 1990).

$$\chi_{fd}\% = \frac{\chi_{lf} - \chi_{hf}}{\chi_{lf}} \times 100\% , \tag{1}$$

Hysteresis, first-order reversal curve (FORC) diagrams, and isothermal remanent magnetization (IRM) acquisition curves were studied through a MicroMag 8600 Series Vibrating Sample Magnetometers (MicroMag 8600 VSM) to assess both

100 mineralogy and magnetic grain size in the Key Laboratory of Paleomagnetism and Tectonic Reconstruction, Ministry of Natural Resources at the Institute of Geomechanics, Chinese Academy of Geological Sciences. In addition, the FORC diagrams were calculated using a FORCinel v3.06 software (Harrison and Feinberg, 2007) (https://wserv4.esc.cam.ac.uk/nanopaleomag). Furthermore, analysis of FORC diagrams plays a key role in indicating domain state and hence magnetic particle grain size, and identification of magnetic interactions between the magnetic grains

105 in the sample (Kodama, and Hinno, 2014).

The colors of the samples were measured with a colorimeter (Konica Minolta Chroma Meter CR400) in the Key Laboratory of Active Tectonics and Geological Safety, Ministry of Natural Resources at the Institute of Geomechanics, Chinese Academy of Geological Sciences. The samples were dried out at room temperature for 5 days before this measurement. The colors of samples were recorded according to the Commission Internationale de l'Eclairage (CIE) 1976 color space including

110 L^*, a^*, and b^* values. L^* is lightness which corresponds to black ($L^* = 0$) and white ($L^* = 100$), a^* is red which corresponds to red ($a^* > 0$) and green color ($a^* < 0$), b^* is yellow which corresponds to yellow ($b^* > 0$) and blue color ($b^* < 0$) (Hunt, 1980).

Grain size parameters were measured using a Malvern Mastersizer 2000 in the Key Laboratory of Active Tectonics and Geological Safety, Ministry of Natural Resources at the Institute of Geomechanics, Chinese Academy of Geological Sciences. Grain size distribution and statistic parameters were calculated using Mastersizer 2000 software

115 (https://www.malvernpanalytical.com/en/support/product-support/mastersizer-range/mastersizer-2000) and Excel. Furthermore, grain size unmixing and analysis were calculated using an AnalySize software v1.2.1 (Paterson and Heslop, 2015) (https://github.com/greigpaterson/AnalySize/releases). The grain size parameters (including mean grain size (M_z), standard deviation (σ_1), skewness (SK_1), and kurtosis (K_G)) have been computed based on data obtained from the cumulative curves, as suggested by Folk and Ward (Folk and Ward, 1957; Folk, 1966; Folk, 1980) according to equation (2) - (5)

120 respectively,

$$M_Z = \frac{\Phi_{16} + \Phi_{50} + \Phi_{84}}{3} , \tag{2}$$

$$\sigma_1 = \frac{\Phi_{84} - \Phi_{16}}{4} + \frac{\Phi_{95} - \Phi_{15}}{6.6} , \tag{3}$$

$$SK_1 = \frac{\Phi_{16} + \Phi_{84} - 2\Phi_{50}}{2(\Phi_{84} - \Phi_{16})} + \frac{\Phi_5 + \Phi_{95} - 2\Phi_{50}}{2(\Phi_{95} - \Phi_5)} , \tag{4}$$

$$K_G = \frac{\Phi_{95} - \Phi_5}{2.44(\Phi_{75} - \Phi_{25})} . \tag{5}$$

125 Five samples were observed to visualize grain specific traits and characterize the relative abundance of existing elements and corresponding atomic proportions using scanning electron microscope (SEM) and energy dispersive spectrometer (EDS) at the Key Laboratory of Shale Oil and Gas Geological Survey, Chinese Academy of Geological Sciences using a Zeiss Sigma 300 scanning electron microscope. In order to achieve high-quality photographs, all samples were coated with tiny carbon particles before the experiments.

4 Results

4.1 Sedimentary characteristics

The profile Pala is about 300cm thick (Fig. 2 a and b). Fine brownish sands were observed visually at about 0-40 cm depth, and slight soil formation processes occurred at this depth interval. The sands were dominated by light brownish sand with few gravels at a depth of 40 to 300 cm (Fig. 3). These scattered gravels were observed at 22cm (Fig. 3 a), 127cm (Fig. 3 b),
135 130cm (Fig. 3 c), 136cm (Fig. 3 d), and 151cm (Fig. 3 e) depth. Such gravels are dominated by feldspar and a bit of gneiss (red dotted circle, Fig. 3 e). The longest diameter of the gravels is nearly 15 mm in diameter at 48 cm depth. In general, the former is finer than the latter. The sedimentary bedding was not found in the aeolian sands of this profile.

The SEM photographs of representative samples at the different depths are shown in Figure 3 f-k. Many of grains show fragments of angular grains with aeolian abrasion limited to corners and edges (Fig. 3 f, g, i, and j). Nevertheless, the
140 surfaces of other grains exhibit an angular shape with sharp edges and corners (Fig. 3 h). The EDS spectrums taken at the labeled spots from Figure 3 f and Figure 3 h show the presence of Si, O, Na, Al, K, and C (from carbon coated particles) (Fig. 3 l and m). Furthermore, an elements profile for sands from representative sample S-85 at 270 cm depth is shown in Fig. 8 k. It can be seen that Si, O, Na, Al, and C (from carbon coated particles) were detected. The profile of the elements (Fig. 3 k) has the same or similar mineral composition with the elements obtained from spots (Fig. 3 l and m). The EDS analysis of
145 representative samples implies the presence of feldspar. This is consistent with the results from gravels (Fig. 3 a-e).

4.2 Chronology

In order to understand the sedimentary time of aeolian sediments, a total of 4 samples were used for OSL dating in the Profile Pala. As shown in Table 1, OSL dating of 4 samples had ages of 11.0±1.5 ka B.P., 11.0±1.2 ka B.P., 8.6±0.9 ka B.P., and 5.5±0.6 ka B.P. at 260cm, 160cm, 80cm, and 30cm depths respectively. According to the dating results, two age-depth
150 model are built based on 4 OSL dating data to estimate the relationship between age and sedimentation of aeolian sediments (Fig. 2 a). It's important to note that the linear fitting model 1 (y=23.28x-104.77) hardly applies to the top of the profile because it possibly has suffered flowing water erosion and wind erosion. The linear fitting model 2 (x=11), meanwhile, is also not applied to the bottom of the profile because it has not enough dating data constraints.

Table 1. OSL dating results of the Profile Pala (28°18′57″ N, 87°25′26″ E, 4325 m elevation)

Sample ID	Depth (cm)	Mineral	Dose Rate (Gy/ka)	De (Gy)	External U (ppm)	External Th (ppm)	External K (%)	Water content(%)	Age (ka)
S1997-1	30	Quartz	4.510±0.186	24.79±2.50	3.79	21.1	2.4	15±5	5.5±0.6
S1997-2	80	Quartz	4.339±0.180	37.38±3.62	3.79	21.1	2.4	15±5	8.6±0.9
S1997-3	160	Quartz	4.078±0.170	44.97±4.64	3.12	20	2.31	15±5	11.0±1.2
S1997-4	260	Quartz	3.540±0.152	38.77±5.18	2.24	14.7	2.29	15±5	11.0±1.5

155 **4.3 Magnetic properties**

Magnetic parameters and plots for the profile Pala are plotted in Figure 4 a-b and Figure 5 a-f. IRM acquisition curves of typical samples present an obvious contrast between the depths of 40-0cm and 283-40 cm, and IRM of the former is higher than the latter (Fig. 4 a). Most of these IRM curves acquired at 1 T and 2 T maximum field show a rapid increase near magnetic saturation at a field of about 200-300 mT. Only the sample S-9 at 16 cm depth and sample S-13 at 24 cm depth

160 reach saturation at about 500 mT. And the saturation isothermal remanent magnetization (SIRM) of these samples range from 0.18 Am^2 kg^{-1} to 0.88 Am^2 kg^{-1} (Fig. 4 a). Such results indicate that the presence of a low coercivity, ferrimagnetic mineral assemblage (e.g., magnetite or maghemite) existed in the samples of the entire profile Pala.

As shown in Figure 4 b and Figure 5 b-d, magnetic parameters can be garnered from a hysteresis plot of 18 typical samples and hysteresis plot of 7 typical samples from top to bottom at profile Pala. The coercivity (H_c) of these samples was less than

165 0.25 mT (Fig. 5 b). The saturation magnetization (M_s) values of 18 typical samples range from 6.20 Am^2 kg^{-1} to 24.86 Am^2 kg^{-1} (Fig. 5 c), and exhibited a roughly increasing trend from bottom to top at profile Pala. The situation of very low coercivity and narrow shape of representative normalized hysteresis plot (Fig. 4 b) illustrates that samples of profile Pala had a character of multi-domain (MD) grains. To put these results of coercivity to the test, three representative samples were selected for FORC diagrams. The H_u and H_c were set to (-50 mT, 40 mT) and (0 mT, 60 mT) respectively according to the

170 pattern of the saturation hysteresis loop. A series of open contours that run nearly parallel to the H_u axis in FORC diagrams (Pike et al.,2001; Qin et al.,2008) of three samples indicate that there is the presence of MD grains with very low coercivity at these samples (Fig. 4 c-e). This observation is consistent with the results from magnetic parameters and hysteresis. In general, magnetic mineral species and grain size of profile Pala are little changed.

The χ_{lf} values range from 9.4×10^{-8} m^3 kg^{-1} to 33.0×10^{-8} m^3 kg^{-1}, with a mean of 14.47×10^{-8} m^3 kg^{-1}. Meanwhile, the values

175 of χ_{lf} show an abrupt increase at depth of 40-0 cm, indicating the presence of slight soil formation processes (Fig. 5 f). The χ_{fd}% values range from -3.91% to 5.77%, and show that the abrupt decrease at 261-242 cm, 231-210 cm, 188-130 cm, and 40-0 cm depths, which divided the variation process of χ_{fd}% values into four stages (Fig. 5 g).

4.4 Color variations

The profile Pala of L*, a*, and b* values of the sediments are plotted in Figure 5 g-i. L*, a*, and b* values have a significant

180 variation with depth, and these variations are marked by a very sharp decrease of the L* values. The main reason for such variations is the presence of slight soil formation processes at the top (0-40 cm depth) of the profile. L* values at 40-283 cm

depth show that the abrupt increase at 264-242 cm, 231-210 cm, and 189-169 cm, 158-130 cm depths (Fig. 5 g). Such variations show that there is a totally different trend between L^* values and $\chi_{fd}\%$. The b^* values and L^* values have a similar tendency with variations of depths apart from the 0-40 cm depth (Fig. 5 i). These a^* values are similar to b^* values, and they
185 all increase abruptly at 0-40 cm depth (Fig. 5 h).

4.5 Grain-size characteristics

The mean grain size (M_z) reflects the concentration of grain size distribution (Zhu, 2008). As shown in Fig. 6 a, the mean grain size ranges from 90.71 μm to 230.65 μm, which indicates that the sediments of profile Pala were mainly composed of very fine sands (63 μm-125 μm) to fine sands (125 μm-250 μm) (Wooden-Windard Grain Standard). The 63-125 μm grains
190 percentage ranges from 8.85% to 28.91% (average 18.63%), and has a maximum (28.91%) at 65cm depth (Fig. 6 d). The 125-250 μm grains have a content of 26.58%-44.9% (average 36.53%), and the maximum is 38.76% at 164 cm depth (Fig. 6 e). The percentage of 250-500 μm grains ranges from 12.33% to 38.76% (average 22.53%), and reached 38.76% (maximum) at 133 cm depth (Fig. 6 f).

It is worth noting that the percentage of 250-500 μm grains occurs an abrupt increase at 264-244 cm, 231-210 cm, 189-170
195 cm,160-130 cm, and 40-0 cm depths, which divided the variation process into four stages. The standard deviation (σ_1) represents the uniformity of grain size (Zhu, 2008). The values of standard deviation were 1.20-1.87 (Fig. 7 a), with an average of 1.49. Though the distribution of the grains is fine sands, they are poorly sorted. The skewness (SK_1) is used to understand the formation mechanism of sediments and to measure the non-normality of a grain size distribution (Folk, 1966; Zhu, 2008). The coefficient of skewness ranges from 0.10 to 0.49 (Fig. 7 a), which reflects that the frequency curves are
200 positive-skewed (0.1-0.3) and very positive-skewed (0.3-1) (Folk, 1966). A "tail" of fines appears in the frequency curves (Fig. 7 b). Furthermore, the positive skew distribution is an indication that the abundance of grain size in the fine fraction is greater than the abundance of grain size in the coarse fraction. Kurtosis (K_G) is measured to the sharp shape of grain size frequency distribution curves (Zhu, 2008). Kurtosis values are 1.26-2.13, with an average of 1.59 (Fig. 7 a), which indicates that the frequency curves are leptokurtic (1.11-1.56) and very leptokurtic distributions (1.56-3.00) (Folk, 1966; Zhu, 2008).
205 In order to unmix the different contents from grain size distribution (GSD), the AnalySize software v1.2.1 (Paterson and Heslop, 2015) was used to conduct the grain size unmixing. As shown in Figure 7 b, three end numbers (EM) were calculated using an AnalySize. The EM1, EM2, and EM3 have a mean grain size of 97.48 μm, 138.58 μm, 227.56 μm, respectively. The varying curves in the depth of EM (Fig. 6 h-j) illustrate that the abundance of EM3 shows an abrupt increase at 264-244 cm, 231-210 cm, 189-131 cm, and 40-0 cm depths, which divided the variation process of EM3 into four
210 stages (Fig. 6 h). The EM2, meanwhile, marks an opposite trend compared with the EM3 (Fig. 6 i). As shown in Figure 7 c, the probability cumulative curves of representative samples are plotted according to the results of grain size parameters and EM. The content of rolling and saltation grains reach 70%-80%. These suspended grains have a lower content, about 20%-30%. These curves are divided into two major parts by the intersections which correspond to the grain size of 3.0 Φ-3.5Φ (120 μm -90 μm).

5 Discussion

5.1 Sources of aeolian sediments

A "tail" of fines appears in the frequency curves (Fig. 7 b) indicating that the aeolian sediments are composed of fine-grained and coarse-grained sources. Observations from investigating and SEM-EDS suggest that aeolian sediments are composed mainly of feldspar grains and gravels (Fig. 3). This could be explained by the glaciation in the Himalayan Mountains and weathering of exposed bedrocks and glacial deposits. In Pala and its surrounding upland, exposed strata are dominated by monzogranite and Meso-and Neoproterozoic Zhaxirega Formation-complex (mainly composed of gneiss, granulite, migmatite, and migmatitic gneiss) (Fig. 1 b). Since the Last Glacial Period (LGP), these exposed bedrocks might yield a mass of glacial deposits including gravels, sands, and muds under the action of glaciation. Meanwhile, smaller pieces had been yielded under the weathering in these glacial deposits and other exposed bedrocks (Wicander and Monroe, 2017). Further, glacial deposits, monzogranite, gneiss, and other feldspathic rocks in Pala and the surrounding area yielded these smaller pieces of the individual feldspar, and provide the sources for aeolian sediments.

Results of surface characteristics show that scattered angular gravels (Fig. 3 a-e) and angular feldspar grains (Fig. 3 f-m) in aeolian sediments had not experienced distant transportation. These grains were transported by the way of rolling and saltation (＞125 μm) (Fig. 7 c) under the wind force. Gravels rolled down the slope under wind force and their own gravity and deposited finally. In summary, such available evidence suggests that these glacial deposits and weathering products of bedrocks and glacial deposits near the Pala provide a major local-field source of aeolian sediments to Pala and the surrounding area. It is worth noting that magnetic particles were transported along with fine-grained clay or dust by the wind force from a potential far-field with a suspended way (Han et al., 1997) and deposited finally. In profile Pala, little changed species of magnetic minerals (Fig. 4 and 5 a-d) in aeolian sediments suggest the existence of a single far-field source area for suspended particles.

Based on these observations, furthermore, regional geological and geographic setting, and characteristics of aeolian sediments, there are three plausible sources including local-field and far-field that could provide sediments for Pala and its surrounding area: 1) Glaciers retreating in Pala and surrounding uplands since the end of the Last Glacial Maximum (LGM) could expose large glacial sediments, providing a potential local-field coarse and far-field source of aeolian sediments to Pala. 2) Weathering products of bedrock in Pala and the surrounding uplands could also provide a potential local-field coarse source of aeolian sediments to Pala. 3) Dry and windy conditions and lack of vegetative cover could expose surface sediments, providing potential far-field and local-field sources of aeolian sediments to Pala.

5.2 Aeolian records and changes in Indian monsoon intensity

Proxy records, dominatingly including planktic foraminifera Globigerina bulloides abundance (G. bulloides) from the Arabian Sea (Gupta et al., 2005; Gupta et al., 2013; Das et al., 2017), $\delta^{18}O$ from speleothem and lake (Fleitmann et al., 2003; Dykoski et al., 2005; Cai et al., 2012; Henderson et al.,2013), $\delta^{13}C$ from peat bog (Hong et al., 2003) are used to reflect the

change of Indian monsoon intensity. These proxies are mainly preserved in the marine, speleothem, and lake. However, these records are rare in the northern slope of the Himalayan Mountains. In this study, we interpret the percentage of 250-500 μm grains to reflect the change of Indian monsoon intensity based on the following reasons:

250 1) Unlike clays and silts (<63 μm) and fine sands (63-250 μm), the percentage of 250-500 μm grains is a more sensitive indicator of the rolling and saltation grains in aeolian sediments (Fig. 7 c) because their transportation and accumulation depend on the stronger winds.

2) Surface characteristics of gravels and grains indicate that these rolling and saltation grains had not experienced distant transportation, and mainly came from the local-field source, such as glacial deposits, weathering products from exposed
255 bedrocks and glacial deposits.

3) The Pala is sensitive to the component of rolling and saltation because of its regional geography, especially for the 250-500 μm grains. In geomorphic structure, the Pala is situated on an upland (Fig. 1 c), its vertical elevation difference with the northeast riverbed and southwest riverbed is more than 300 m and 500 m respectively. Further, the wind force is decisive to the transportation of 250-500 μm grains.

260 As shown in Figure 8 e-g, the change of percentage of 250-500 μm grains is good in agreement with the Indian monsoon intensity which is reconstructed by marine proxy from the Arabian Sea (Gupta et al., 2005; Gupta et al., 2013; Das et al., 2017) and the speleothem records from Dongge Cave (Dykoski et al., 2005) (Fig. 8 e-g). Given these observations and reasons, we suggest that the percentage of 250-500 μm grains is a sensitive proxy for the change in Indian monsoon intensity in Pala.

265 **5.3 Indian monsoon oscillation, aeolian activity, and process of desertification**

On the basis of OSL dating, characteristics of these parameters (i.e., grain-size characteristics, color variations, and magnetic properties) in aeolian sediments, sources of aeolian sediments, changes in Indian monsoon intensity, and other factors, the aeolian processes, climatic changes, and regional processes of desertification are divided into three subunits during the Early-Mid Holocene.

270 **5.3.1 Unit 1: ~11 - 9.6 ka B.P.**

Four abrupt increases in the percentage of 250-500 μm grains occur between ~11 and 9.6 ka B.P., reaching a maximum at ~10 ka B.P.. The four abrupt strengthening intervals of the percentage of 250-500 μm grains appeared between ~12 and 11 ka B.P. (a treble event), and between 10.6 and 9.6 ka B.P.. (Fig. 8 e). These abrupt strengthened intervals suggest that Indian monsoon intensity strengthened abruptly from ~12 to 11 ka B.P. (a treble event, Subunit 1-3) and 10.6 to 9.6 ka B.P.
275 (Subunit 4), and with the strongest conditions at ~10 ka B.P.. This is consistent with the changes of Indian monsoon intensity from the marine proxies (G. bulloides) in the Arabian Sea (Fig. 8 f) (Gupta et al., 2005; Gupta et al., 2013; Das et al., 2017) and δ^{18}O from speleothem proxies in China (Dykoski et al, 2005; Cai et al., 2012) and Oman (Fleitmann et al., 2003). The enhanced Indian monsoon may be caused by an increase in solar radiation from ~11 to 9.6 ka B.P. (Fig. 8 f) (Fleitmann et al.,

2003; Dykoski et al., 2005; Zhu et al., 2015). In addition, the appearance of these scattered angular gravels in aeolian
280   sediments (Fig. 3 b-e) is coincident with the stronger intensity of the Indian monsoon between 10.6 and 9.6 ka B.P. (Subunit
4).

It is worth noting that the percentage of 0-63 μm grains is lowest in Subunit 1, Subunit 2, Subunit 3, and Subunit 4.
Meanwhile, the low values of χ_{lf} (Fig. 8 a) respond well to these four subunits (Fig. 8 b). This is because the component of 0-
63 μm and magnetic minerals hardly deposit under the influence of stronger wind or they could be removed by the stronger
285   wind (Wicander and Monroe, 2017). However, the overall values of χ_{lf} between ~11 and 9.6 ka B.P. are lower than the
overall values of χ_{lf} between 9.6 and 6.3 ka B.P.. This difference of χ_{lf} could be explained by the change in climate and
Indian monsoon intensity. The high lake level in Peiku Co (Wuennemann et al., 2015), climatic reconstruction using
canonical correspondence analysis (CCA) based on pollen data in Chen Co (Lu et al., 2011), reconstruction of summer
temperature in Tibetan Plateau (Shi et al., 2021), and pollen records from Peiku Co, Chen Co, and Nariyong Co (Huang,
290   2000; Lu et al., 2011; Tang et al., 2021) (Fig. 1 a) demonstrate that climatic conditions were warm and dry, and the alpine
meadow vegetation or alpine shrub meadow vegetation occurred in these areas from Peiku Co to Chen Co between ~11 and
9.6 ka B.P.. Less accumulation of magnetic minerals because the warm and dry climate inhibits the pedogenic process (Zhou
et al., 1990; Deng et al., 2005; Liu et al., 2005; Liu et al., 2007) and sparse vegetation cover disenables dust and magnetic
minerals trapping (Huang et al.,2021). The most important force dominating the values of χ_{lf} the was the change in Indian
295   monsoon intensity. The appearance of higher values of L^* is coincident with the strengthening Indian monsoon intensity
between ~11 and 9.4 ka B.P., this may be strongly associated with the increasing coarse grains.

About 165 cm of aeolian sediments had deposited rapidly between ~11 and 9.6 ka B.P., and the average percentage of ＞125
μm grains is greater than 69.6 % (Fig. 6 b-f). This rapid deposition suggests that a strengthened aeolian activity from ~11 to
9.6 ka B.P., and a peak of aeolian activity at ~10 ka B.P. is recorded. The rapid accumulation of sediments is dominated by
300   the fine sands and more coarse-grained, and has a positive response to the general strengthening of Indian monsoon intensity.
However, it may be implausible to attribute the rapid accumulation of aeolian sediments to the strengthening of Indian
monsoon intensity. Further, this aeolian activity is most likely induced by the combined effects of climate, vegetation cover,
and sources, monsoon. A warm, dry, and windy environment with sparse alpine meadow vegetation cover could expose the
glacial sediments and weathering products, generating a widely distributed source, and the strengthened Indian monsoon
305   accelerated the aeolian activity. Further, the desertification and aeolian activity caused by a warm, dry, and windy
environment, and sparse vegetation cover were not just limited to Pala, but also existed in the Dinggye area, about 40 km
northeast of Pala, between ~11 and 9.6 ka B.P. (Pan et al., 2014).

5.3.2 Unit 2: 9.6 - 6.3 ka B.P.

Although the marine proxies (G. bulloides) in the Arabian Sea (Fig. 8 f) (Gupta et al., 2005; Gupta et al., 2013; Das et al.,
310   2017) and $\delta^{18}O$ from speleothem proxies in China (Dykoski et al, 2005; Cai et al., 2012) and Oman (Fleitmann et al., 2003)
indicate that the Indian monsoon intensity occurred three strengthening events between ~9.6 and 6.3 ka B.P. (Fig. 8 f) and

three weakening events (9.2 ka B.P., 8.2 ka B.P., and 8.1 ka B.P.) (Fig. 8 g), the percentage of 250-500 μm grains generally declines between 9.6 and 6.3 ka B.P. (Fig. 8 e). Moreover, the small increasing percentage of 250-500 μm grains (Fig. 8 e) and L^* (Fig. 8 b) response to the strongest intensity of the Indian monsoon (Fig. 8 f) between ~8.6 and 8.2 ka B.P..

315 However, the general decline in values of χ_{lf} (Fig. 8 a) does not respond to the change of the Indian monsoon intensity between ~11 and 9.6 ka B.P.. After ruling out the influence of change in the Indian monsoon intensity, the climate, and vegetation cover may dominate the general decline in values of χ_{lf}. The evidence from climatic reconstruction in Chen Co (Lu et al., 2011), reconstruction of summer temperature in the Tibetan Plateau (Shi et al., 2021), and pollen records from Peiku Co, Chen Co, and Nariyong Co (Huang, 2000; Lu et al., 2011; Tang et al., 2021) (Fig. 1 a) suggest that these areas

320 from Peiku Co to Chen Co were dominated by the warm and humid climate between 9.6 and 6.3 ka B.P.. A gradual transition of vegetation from alpine shrub meadow to coniferous and broadleaved mixed forest occurred between ~9.6 and 8 ka B.P., and the forest-shrub meadow landscape appeared between ~8 and 6.3 ka B.P. (Huang, 2000; Lu et al., 2011; Tang et al., 2021). Further, there are four ways in which the general decline in values of χ_{lf} could be caused: 1) The weakened Indian monsoon intensity is more beneficial to the deposition of magnetic minerals; 2) Rich vegetation cover enables dust and

325 magnetic minerals trapping (Huang et al.,2021); 3) Warm and humid climate, comparative low sedimentation rate, and increased fine-grained component is favorable to the pedogenic process, generating a transition of magnetic minerals in sediments from magnetite to maghemite (Zhou et al., 1990; Deng et al., 2005; Liu et al., 2005; Liu et al., 2007); 4) The increased precipitation enables the trapping of magnetic minerals and dust in warm and humid climatic conditions. Unlike the change observed in χ_{lf}, the declined percentage of 250-500 μm grains between 9.6 and 6.3 ka B.P. is most likely caused

330 by the increased vegetation cover. The increased vegetation cover could result in decreased source and reduce the input of rolling and saltation grains, and overwrite the record in aeolian sediments from the change of Indian monsoon intensity.

About 80 cm of aeolian sediments had deposited between 9.6 and 6.3 ka B.P., and the content of ＞125 μm grains ranges from 52.81% to 57.75%, with an average of 54.51%. The EM3 also presents a decreased trend (Fig. 6 j). This comparatively slow deposition suggests that a weakened aeolian activity from ~9.6 to 6.3 ka B.P.. Further, this weakened aeolian activity is

335 mostly induced by the effect of vegetation cover. A warm and humid climate with rich vegetation cover reduces the exposure of local-field source and far-field source, and the input of rolling and saltation grains. Meanwhile, the process of desertification tends to weaken between 9.6 and 6.3 ka B.P.. In the Dinggye area, the typical sandy paleosol was developed rather than strengthened aeolian activity (Pan et al., 2014) because of the different sources between the Dinggye area and Pala. The source in the Dinggye area is mainly from the fluvial sediment in the Pum Qu, but the glacial sediments and

340 weathering products provide the main source to Pala.

5.3.3 Unit 3: 6.3 - ~ 4.5 ka B.P.

The content of 250-500 μm grains increases slightly between 6.3 and ~4.5 ka B.P. (Fig. 8 e) and is likely caused by the strengthened Indian monsoon intensity (Fig. 8 f). However, the increasing content of 0-63 μm grains is not consistent with the strengthened Indian monsoon in this period (Fig. 8 d), which implies that the fine-grained silt and clay were formed

345 during the pedogenic process in post-deposition. Meanwhile, the values of χ_{lf} (Fig. 5 e) dramatically increase between 6.3 and ~4.5 ka B.P., attaining more than twice the values of Unit1 and Unit 2. The high values of χ_{lf} imply an effect of the pedogenic process because of generating a transition of magnetic minerals in sediments from magnetite to maghemite (Zhou et al., 1990; Deng et al., 2005; Liu et al., 2005; Liu et al., 2007). Moreover, this effect of the pedogenic process also overwrites the raw information of color variations in aeolian sediments (Fig. 5 g-i).

350 The warm and humid climate with comparative rich vegetation cover still dominated between 6.3 and ~4.5 ka B.P. (Huang, 2000; Lu et al., 2011; Tang et al., 2021), but the temperature and humidity had declined relative to Unit 2 (Lu et al., 2011; Shi et al., 2021). In general, comparative warm and humid climate and rich vegetation cover, and less exposure in source further inhibit the aeolian activity and development of desertification.

5.4 Implications for paleoclimate and paleoenvironment

355 Differences in sedimentary and climatic records could be caused by different sources and different landforms in the same region. The sources from fluvial sediments likely had a lagged record in paleoclimate and paleoenvironment because the vegetation cover hard to influence the supplies of fluvial sediments in aeolian activity. However, the record from aeolian sediments bypasses this problem. In addition, the river terraces (e.g., Dinggye area) and uplands (e.g., Pala) have different responses to climate change.

360 Further, climate changes are crucial to the aeolian activity and development of desertification. It is evident from aeolian sediments in the Pala and Dinggye area results that a dry climate with sparse vegetation cover could trigger desertification. Significantly, little and sparse vegetation cover exposes more sources, and the strengthened monsoon likely further accelerates the aeolian activity. On the other hand, although these glaciers had retreated since the LGM due to climate change, abundant glacial sediments were generated. Meanwhile, these glacial sediments and weathering products derived

365 from bedrocks and glacial sediments could provide sources to aeolian sediments. As the change of climate, the humid and warm environment with increased and rich vegetation cover could decline the exposure of glacial sediments and weathering products, and further inhibit the aeolian activity and desertification. In general, the change of the paleoenvironment lagged behind the paleoclimate because of the belated vegetation cover, especially in the northern slope of the middle Himalayan Mountains.

6 Conclusions

The potential connection between aeolian sediments, climatic changes, and environmental changes during the Holocene in the southern slope of the Himalayan Mountains is important to understand the climatic and ecological systems of the Tibetan Plateau and Southern Asia. Combining the OSL dating, sedimentary characteristics, magnetic parameters, grain size parameters, and color variations, we constrain the sources of aeolian sediments in Pala and change in Indian monsoon

375 intensity based on the aeolian sediments proxy and other records (Dykoski et al., 2005; Gupta et al., 2005; Gupta et al., 2013;

Das et al., 2017). Three plausible local-field and far-field could provide sources for Pala and its surrounding area during the Early-Mid Holocene in the southern slope of the Himalayan Mountains, including glacial sediments, weathering products of bedrock and glacial sediments, and exposed surface sediments. Further, the linkages between Indian monsoon oscillation, aeolian activity, and the process of desertification is identified based on the above evidence and can be subdivided into three

380 subunits. First, the strengthened Indian monsoon intensity, dry and warm climate, and sparse vegetation cover accelerated the rapid expansion of desertification between ~11 and 9.6 ka B.P.. The second subunit of decelerated desertification was identified in the weakened Indian monsoon intensity, warm and humid climate, and increased vegetation cover between 9.6 and 6.3 ka B.P.. Third, influenced by the weakened Indian monsoon intensity, warm and humid climate, increased vegetation cover, and limited sources, the desertification decelerated further between 6.3 and ~4.5 ka B.P.

385 The linkage and interplay between changes in the Indian monsoon, vegetation cover, sources, and landforms play a key role in aeolian processes and regional processes of desertification in the northern slope Himalayan Mountains during the Early-Mid Holocene. Our findings indicate that differences in sedimentary and climatic records could be produced by different sources and different landforms in the same region, and further indicate that climate changes are crucial to the aeolian activities and development of desertification. Moreover, paleoenvironmental changes during the Holocene lagged behind the

390 changes in paleoclimate because of the belated vegetation cover in the northern slope of the middle Himalayan Mountains.

Data availability

The dataset for grain-size parameters, magnetic parameters, and color variations will be made available on the public data repository Science Data Bank.

Author contribution

395 Yao Gao participates to the conceptualization, investigation, writing, and methodology. Keqi Zhang participates to the investigation (OSL), conceptualization, methodology, and validation. Zhonghai Wu provides the funding acquisition, and participates to the conceptualization, methodology, and supervision. Tingting Tian participates to the sampling of all laboratory samples, and investigation (SEM-DES). Hailong Gai and Jiameng Zuo participate to the sampling of all laboratory samples. Bin Li participates to the editing (pictures). Yao Gao prepared the manuscript with contributions from all

400 co-authors.

Competing interests

The authors declare that they have no conflict of interest.

Acknowledgments

This work was supported by the National Natural Science Foundation of China (Grant Nos. U2002211). We would like to
405 thank Dr. Shifeng Wang for his help, Dr. Chaozhu Li for his excellent technical support with the grain size distribution
experiments, magnetic susceptibility experiments, and colors variations experiments at the Key Laboratory of Active
Tectonics and Geological Safety, Ministry of Natural Resources at the Institute of Geomechanics, Chinese Academy of
Geological Sciences in 2021, and Bingqian Wang for his assistance with the operation of SEM.

References

410 Alivernini, M., Lai, Z., Frenzel, P., Fuerstenberg, S., Wang, J., Guo, Y., Peng, P., Haberzettl, T., Börner, N., and Mischke, S.:
Late quaternary lake level changes of Taro Co and neighbouring lakes, southwestern Tibetan Plateau, based on OSL dating
and ostracod analysis. Global and Planetary Change, 166, 1-18, https://doi.org/10.1016/j.gloplacha.2018.03.016, 2018.

An, Z., Colman, S. M., Zhou, W., Li, X., Brown, E. T., Timothy, A. J., Cai, Y., Huang, Y., Lu, X., Chang, H., Song, Y., Sun,
Y., Xu, H., Liu, W., Jin, Z., Liu,, X., Cheng, P., Liu, Y., Li, X., Liu, X., Yan, L., Shi, Z., Wang, X., Wu, F., Qiang, X., Dong,
415 J., Lu, F., and Xu, X.: Interplay between the Westerlies and Asian monsoon recorded in Lake Qinghai sediments since 32 ka.
Sci Rep 2, 619. https://doi.org/10.1038/srep00619, 2012.

An, Z., Kutzbach, J. E., Prell, W. L., and Porter, S. C.: Evolution of Asian monsoons and phased uplift of the Himalaya-
Tibetan Plateau since late Miocene times. Nature, 411(6833), 62-6, http://dx.doi.org/10.1038/35075035, 2001.

Armijo, R., Tapponnier, P., Mercier, J. L., and Han, T.: Quaternary extension in southern Tibet: Field observations and
420 tectonic implications. Journal of Geophysical Research: Solid Earth, 91(B14): 13803-13872,
https://doi.org/10.1029/jb091ib14p13803, 1986.

Cai, Y., Zhang, H., Cheng, H., An, Z., Edwards, R. L., Wang, X., Tan, L., Liang, F., Wang, J., and Kelly, M.: The Holocene
Indian monsoon variability over the southern Tibetan Plateau and its teleconnections. Earth & Planetary Science Letters,
335-336:135-144, https://doi.org/10.1016/j.epsl.2012.04.035, 2012.

425 Cui, X., and Graf, H. F.: Recent land cover changes on the Tibetan plateau: a review. Climatic Change, 94: 47-61.
https://doi.org/10.1007/s10584-009-9556-8, 2009.

Das, M., Singh, R. K. , Gupta, A. K., and Bhaumik, A. K.: Holocene strengthening of the oxygen minimum zone in the
northwestern Arabian Sea linked to changes in intermediate water circulation or Indian monsoon intensity?.
Palaeogeography, Palaeoclimatology, Palaeoecology. 483,125-135, https://doi.org/10.1016/j.palaeo.2016.10.035, 2017.

430 Deng, C., Vidic, N. J., Verosub, K. L., Singer, M. J., Liu, Q., Shaw, J., and Zhu, R.: Mineral magnetic variation of the
Jiaodao Chinese loess/paleosol sequence and its bearing on long-term climatic variability. Journal of Geophysical Research:
Solid Earth, 110(B3), B03103, https://doi.org/10.1029/2004JB003451, 2005.

Dhital, M. R. (Eds): Geology of the Nepal Himalaya, Springer International Publishing, 2015.

Dong, Z., Hu, G., Qian, G., Lu, J., Zhang, Z., Wang, L., and Lyu, P.: High-Altitude Aeolian Research on the Tibetan Plateau: High-Altitude Aeolian Research. Reviews of Geophysics, 55, 864–901, https://doi.org/10.1002/2017RG000585, 2017.

Dykoski, C.A., Edwards, R.L. Cheng, H., Yuan, D., Cai, Y., Zhang, M., Lin, Y., Qing, J., An, Z., and Revenaugh, J.: A high-resolution, absolute-dated Holocene and deglacial Asian monsoon record from Dongge Cave, China. Earth Planet. Sci. Lett., 233(1-2), 71-86, 10.1016/j.epsl.2005.01.036, 2005.

Fleitmann, D., Burns, S.J., Mudelsee, M., and Neff, U., Kramers, J.: Holocene forcing of the Indian monsoon recorded in a stalagmite from southern Oman. Science, 300(5626), 1737-1739, https://doi.org/ 10.1126/science.1083130, 2003.

Folk, R. L., and Ward, W. C.: Brazos river bar: a study in the significance of grain size parameters. Journal of Sedimentary Research, 27(1), 3-26, https://doi.org/10.1306/74D70646-2B21-11D7-8648000102C1865D, 1957.

Folk, R.L. (Eds): Petrology of sedimentary rocks, Hemphill publishing company, 1980.

Folk, R.L.: A review of grain-size parameters. Sedimentology, 6, 73-93, https://doi.org/10.1111/j.1365-3091.1966.tb01572.x, 1966.

Gadgil, S.: The Indian monsoon and its variability. Annual Review of Earth & Planetary Sciences, 22(1), 429-467. https://doi.org/10.1146/annurev.earth.31.100901.141251, 2003.

Geosyst., 16 (12), 4494-4506, https://doi.org/10.1002/2015GC006070, 2015.

Günther, F., Witt, R., Schouten, S., Mäusbacher, R., Daut, G., Zhu, L., Xu, B., Yao, T., and Gleixner, G.: Quaternary ecological responses and impacts of the Indian Ocean Summer Monsoon at Nam Co, Southern Tibetan Plateau. Quaternary Science Reviews, 112, 66-77. https://doi.org/10.1016/j.quascirev.2015.01.023, 2015.

Gupta, A.K., Das, M., and Andersin, D.M.: Solar influence on the Indian summer monsoon during the Holocene. Geophysical Research Letters, 32(17), 261-261, https://doi.org/10.1029/2005GL022685, 2005.

Gupta, A.K., Mohan, K., Das, M., and Singh, R.K.: Solar forcing of the Indian summer monsoon variability during the Allerod period. Sci. Rep. 3. http://dx.doi.org/10. 1038/srep02753, 2013.

Han, J., Jiang, W., and Chu, J.: Grain size distribution of magnetic minerals in loess and paleosol (in Chinese). Quaternary Sciences. 3, 281-287, 1997.

Harrison, R. J., and Feinberg, J. M.: An improved algorithm for calculating first-order reversal curve (FORC) distributions using locally-weighted regression smoothing, in: AGU Fall Meeting, 2007.

Henderson, A. C., Morellon, M., Ricketts, R. D., Leng, M. J., Holmes, J. A., Olsen, J., Haberzettl, T., and Zhu, L.: Late glacial and Holocene monsoon variability in southern Tibet (Invited), in: AGU Fall Meeting, 2013.

Hong, Y., Hong, B., Hong, Q., Lin, Y., Zhu, Y., Shibata, M., Hirota, M., Uchida, X.T., Leng, H., Jiang, H., and Xu, H.: Correlation between Indian Ocean summer monsoon and North Atlantic climate during the Holocene. Earth Planet. Sci. Lett., 211,371-380, http://dx.doi.org/10.1016/S0012-821X(03)00207-3, 2003.

Huang, F.: Vegetation and climate between 13 ka to 5 ka B.P. in Peiku Co, Tibet (in Chinese). Acta Palaeontol Sin, 39 (3), 441–448, 2000.

Huang, X., Miao, X., Chang, Q., Zhong, J., Mason, J. A., Hanson, P. R., Ou, X., Xu, L., and Lai, Z.: Tibetan dust accumulation linked to ecological and landscape response to global climate change. Geophysical Research Letters, 49, e2021GL096615, https://doi.org/10.1029/2021GL096615, 2022.

470 Hunt, R.W.G.: Color terms, symbols, and their usage. Optical Radiation Measurement, 11-31, 1980.

Immerzeel, W. W., Van Beek, L. P. H. and Bierkens, M. F. P.: Climate change will affect the Asian water towers. Science 328, 1382–1385, https://doi.org/10.1126/science.1183188, 2010.

Kaiser, K., Lai, Z., Schneider, B., Reudenbach, C., Miehe, G., Brückner, H.: Stratigraphy and palaeoenvironmental implications of Pleistocene and Holocene aeolian sediments in the Lhasa area, southern Tibet (China). Palaeogeography,

475 Palaeoclimatology, Palaeoecology 271, 329-342, https://doi.org/10.1016/j.palaeo.2008.11.004, 2009.

Kodama, K. P., and Hinnov, L. A. (Eds): Rock Magnetic Cyclostratigraphy, John Wiley & Sons, Ltd., 2014.

Lai, Z., Kaiser, K., and Brückner, H.: Luminescence-dated aeolian deposits of late Quaternary age in the southern Tibetan Plateau and their implications for landscape history. Quaternary Research, 72(3): 421–430, https://doi.org/10.1016/j.yqres.2009.07.005, 2009.

480 Lekshmy, P. R., Midhun, M., Ramesh, R., and Jani, R. A.: 18O depletion in monsoon rain relates to large scale organized convection rather than the amount of rainfall. Sci Rep 4, 5661. https://doi.org/10.1038/srep05661, 2014.

Li, D.: Dinggye regional geological map, China Geological Survey, Map, 2001a.

Li, D.: Instruction of Dinggye regional geological map, China Geological Survey, Open File Rep., 2001b.

Li, J., Wang, Y., Zhang, L., and Hu, G.: Aeolian desertification in China's northeastern Tibetan Plateau: Understanding the

485 present through the past. Catena, 172, 764-769. https://doi.org/10.1016/j.catena.2018.09.039, 2019.

Li, S., Dong, G., Shen, J., Yang, P., Liu, X., Wang, Y., Jin, H., and Wang, Q.: Formation mechanism and development pattern of aeolian sand landform in Yarlung Zangbo river valley. Science in China Series D: Earth Sciences, 42(3): 272–284. https://doi.org/10.1007/BF02878964, 1999.

Li, T., Wu, Y., Du, S., Huang, W., Hao, C., Guo, C., Zhang, M., and Fu, T.: Geochemical characterization of a Holocene

490 aeolian profile in the Zhongba area (southern Tibet, China) and its paleoclimatic implications. Aeolian Research, 20, 169-175. https://doi.org/10.1016/j.aeolia.2016.01.005, 2016.

Ling, Z., Yang, S., Wang, X., Wang, J., Xia, D., and Chen, F.: Spatial-temporal differentiation of aeolian sediments in the Yarlung Tsangpo catchment, Tibetan plateau, and response to global climate change since the last glaciation. Geomorphology, 357, 107104. https://doi.org/10.1016/j.geomorph.2020.107104, 2020.

495 Liu, Q., Deng, C., Torrent, J., and Zhu, R.: Review of recent developments in mineral magnetism of the Chinese loess. Quaternary Science Reviews, 26(3-4), 368-385, https://doi.org/10.1016/j.quascirev.2006.08.004, 2007.

Liu, Q., Deng, C., Yu, Y., Torrent, J., M. J., Banerjee, S. K., and Zhu, R.: Temperature dependence of magnetic susceptibility in an argon environment: implications for pedogenesis of Chinese loess/palaeosols. Geophysical Journal International 161(1):102-112, https://doi.org/10.1111/j.1365-246X.2005.02564.x, 2005.

500   Lu, H., Wu, N. Q., Liu, K. B., Zhu, L., Yang, X., Yao, T., Wang, L., Li, Q., Liu, X. Q., Shen, C., Li, X., Tong, G. B., and Jiang, H.: Modern pollen distributions in Qinghai-Tibetan Plateau and the development of transfer functions for reconstructing Holocene environmental changes. Quaternary Science Review, 30 (7-8), 947-966, https://doi.org/10.1016/j.quascirev.2011.01.008, 2011.

Lu, R., Jia, F., Gao, S., Li, J., and Zhao, C.: Holocene aeolian activity and climatic change in Qinghai lake basin,
505   northeastern Qinghai–Tibetan plateau. Paleogeography, Palaeoclimatology, Palaeoecology, 430, 1-10. https://doi.org/10.1016/j.palaeo.2015.03.044, 2015.

Molnar, P., Boos, W. R., and Battisti, D. S.: Orographic controls on climate and paleoclimate of Asia: thermal and mechanical roles for the Tibetan Plateau. Annual Review of Earth & Planetary Sciences, 38(1), 77-102. https://doi.org/10.1146/annurev-earth-040809-152456, 2010.

510   Molnar, P., England, P., and Martiod, J.: Mantle dynamics, uplift of the Tibetan Plateau and the Indian monsoon development. Rev. Geophys. 34, 357–396. https://doi.org/10.1029/93RG02030, 1993.

Owen, L.A., Teller, J.T., and Rutter, N.W.: Glaciation and reorganization of Asia's network of drainage Global and Planetary Change, 30, 289-374, 2002.

Pan, M., Wu, Y., Zheng, Y., and Tan, L.: Holocene aeolian activity in the Dinggye area (Southern Tibet, China). Aeolian
515   Research, 12, 19-27, https://doi.org/10.1016/j.aeolia.2013.10.005, 2014.

Paterson, G. A., and Heslop, D.: New methods for unmixing sediment grain size data, Geochem. Geophys.

Pike, C. R. , Roberts, A. P. , Dekkers, M. J. , and Verosub, K. L.: An investigation of multi-domain hysteresis mechanisms using FORC diagrams. Physics of the Earth and Planetary Interiors, 126(1-2), 11-25, https://doi.org/10.1016/S0031-9201(01)00241-2, 2001.

520   Qin, H., Liu, Q., and Pan, Y.: The first-order reversal curve (FORC) diagram: Theory and case study (in Chinese). Chinese J. Geophys., 51(3):743-751, https://doi.org/10.1016/j.chemgeo.2008.02.011, 2008.

Rades, E.F., Hetzel, R., Xu, Q., and Ding, L.: Constraining Holocene lake-level highstands on the Tibetan plateau by 10Be exposure dating: a case study at Tangra Yumco, southern Tibet. Quaternary Science Reviews, 82, 68-77, https://doi.org/10.1016/j.quascirev.2013.09.016, 2013.

525   Shi, F., Lu, H., Guo, Z., Yin, Q., Wu, H., Xu, C., Zhang, E., Shi, J., Cheng, J., Xiao, X., and Zhao, C.: The position of the Current Warm Period in the context of the past 22,000 years of summer climate in China. Geophysical Research Letters, 48, e2020GL091940, https://doi.org/10.1029/2020GL091940, 2021.

Tang, L., Shen, C., Lu, H., Li, C., Ma, Q.: Fifty years of Quaternary palynology in the Tibetan Plateau. Sci. China Earth Sci, 64, 1825–1843, https://doi.org/10.1007/s11430-020-9809-5, 2021.

530   Wang, R., Scarpitta, S. C., Zhang, S., Zheng, M.: Later Pleistocene/Holocene climate conditions of Qinghai-Xizang Plateau (Tibet) based on carbon and oxygen stable isotopes of Zabuye lake sediments. Earth and Planetary Science Letters, 203(1), 461–477, https://doi.org/10.1016/S0012-821X(02)00829-4, 2002.

Wicander, R, Monroe, J. S.: Geology: Earth in Perspective (Third Edition), Cengage Learning, Inc., 2017.

Wu, G., Liu, Y., He, B., Bao, Q., Duan, A., and Jin, F.: Thermal controls on the Asian summer monsoon. Sci. Rep. 2, 404, https://10.1038/srep00404, 2012.

Wuennemann, B., Yan, D., Ci, R.: Morphodynamics and lake level variations at Paiku co, southern Tibetan plateau, china. Geomorphology, 246, 489-501, https://doi.org/10.1016/j.geomorph.2015.07.007, 2015.

Xian, X., Jian, G., Han, B., Sun, Q. W., and Liu, L.: The effect of climate warming and permafrost thaw on desertification in the Qinghai–Tibetan plateau. Geomorphology, 108(3-4), 182-190. https://doi.org/10.1016/j.geomorph.2009.01.004, 2009.

Yao, T., Masson-Delmotte, V., Gao, J., Yu, W., Yang, X., Risi, C., Sturm, C., Werner, M., Zhao, H., He, Y., Ren, W., Tian, L., Shi, C., and Hou, S.: A review of climatic controls on $\delta 18O$ in precipitation over the Tibetan Plateau: Observations and simulations. Reviews of Geophysics, 51(4): 525–548, https://doi.org/10.1002/rog.20023, 2013.

Ye, D., Wu, G.: The role of the heat source of the Tibetan Plateau in the general circulation. Meteorl. Atmos. Phys. 67, 181–198, https://doi.org/10.1007/BF01277509, 1998.

Zhang, J., and Guo, L.: Structure and geochronology of the southern Xainza-Dinggye rift and its relationship to the south Tibetan detachment system. Journal of Asian Earth Sciences, 29(5-6):722-736, https://doi.org/10.1016/j.jseaes.2006.05.003, 2007.

Zhang, J., Guo, L., and Ding, L.: Structural characteristics of middle and southern Xainza-Dinggye normal fault system and its relationship to southern Tibetan detachment system. Chinese Science Bulletin 47, 1063–1069, https://doi.org/10.1360/02tb9239, 2002.

Zhang, K., Qu, J., Han, Q., and An, Z.: Wind energy environments and aeolian sand characteristics along the Qinghai–Tibet railway, china. Sedimentary Geology, 273-274, 91-96. https://doi.org/10.1016/j.sedgeo.2012.07.003, 2012.

Zhou, L., Oldfield, F. A., Wintle, A. G., Robinson, S. G., and Wang, J.: Partly pedogenic origin of magnetic variations in Chinese loess. Nature, 346, 737-739, https://doi.org/10.1038/346737a0, 1990.

Zhu, L., Lü, X., Wang, J., Peng, P., Kasper, T., Daut, G., Haberzettl, T., Frenzel, P., Li, Q., Yang, R., Schwalb, A., and Mäusbacher, R.: Climate change on the Tibetan Plateau in response to shifting atmospheric circulation since the LGM. Sci Rep 5, 13318, https://doi.org/10.1038/srep13318, 2015.

Zhu, X.: Sedimentary petrology (Fourth Edition) (in Chinese). Petroleum Industry Press, 2008.
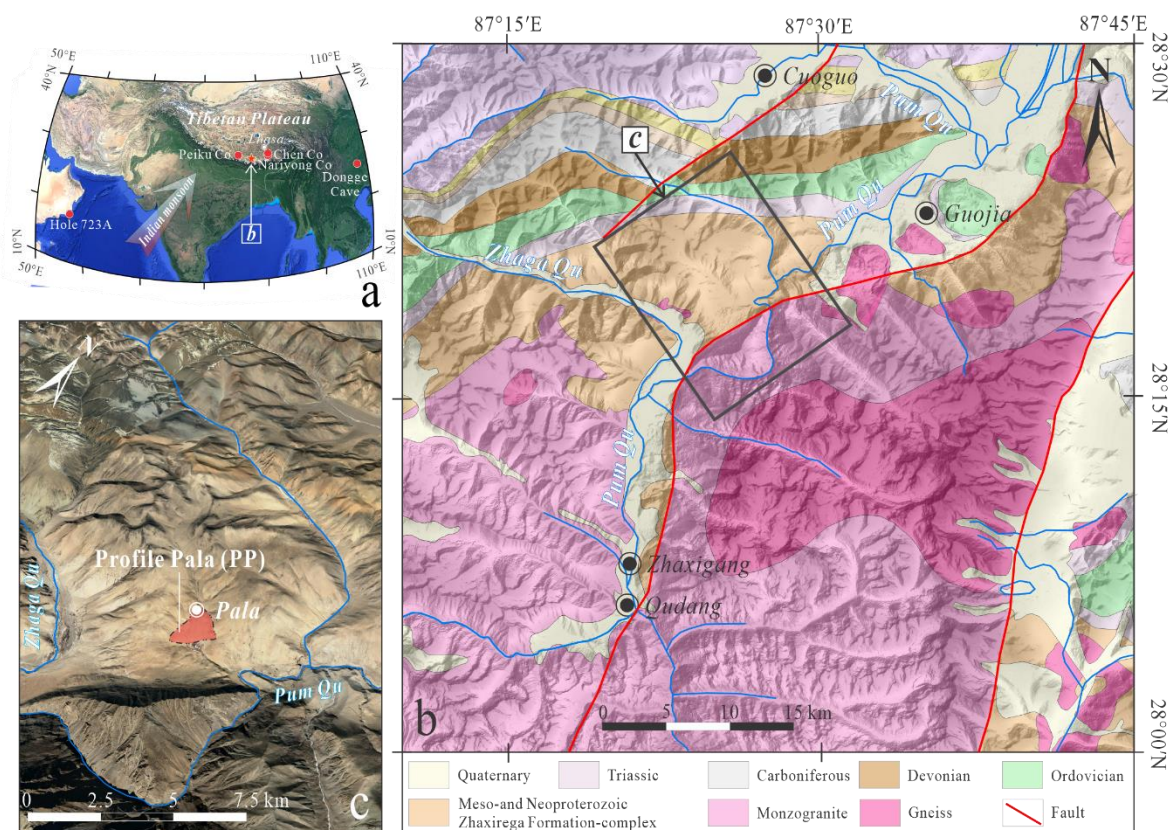
560

Figure 1: Geological setting of this study.

(a) Satellite image by © Google earth of the Tibetan plateau and Himalayas Mountains. Red circles indicate the Dongge Cave (108°5′E, 25°17′ N; 680 m above sea level); Hole 723A (18°3.079′ N, 57°36.561′ E; water depth 807 m), Arabian Sea, Peiku Co (85°37′E, 28°51′N, 4585 m), Chen Co (90°40′E, 28°53′N, 4450 m), and Nariyong Co (90°24′E, 28°34′N, 5020 m). The red five-pointed star indicates the

565   scope of **b**. **(b)** Regional stratigraphic (adapted from the 1:250 000 scale Dinggye regional geological map [H45C004003] (Li, 2001a) (https://geocloud.cgs.gov.cn) and topographic map of the site location. The black box indicates the scope of **c**. **(c)** Three-dimensional (3D) satellite image by © Google earth (data of acquisition: 14 January 2013) of the profile Pala and sampling site. The conjectural area of aeolian sediments is shaded red. The white line indicates the profile Pala and sampling site.
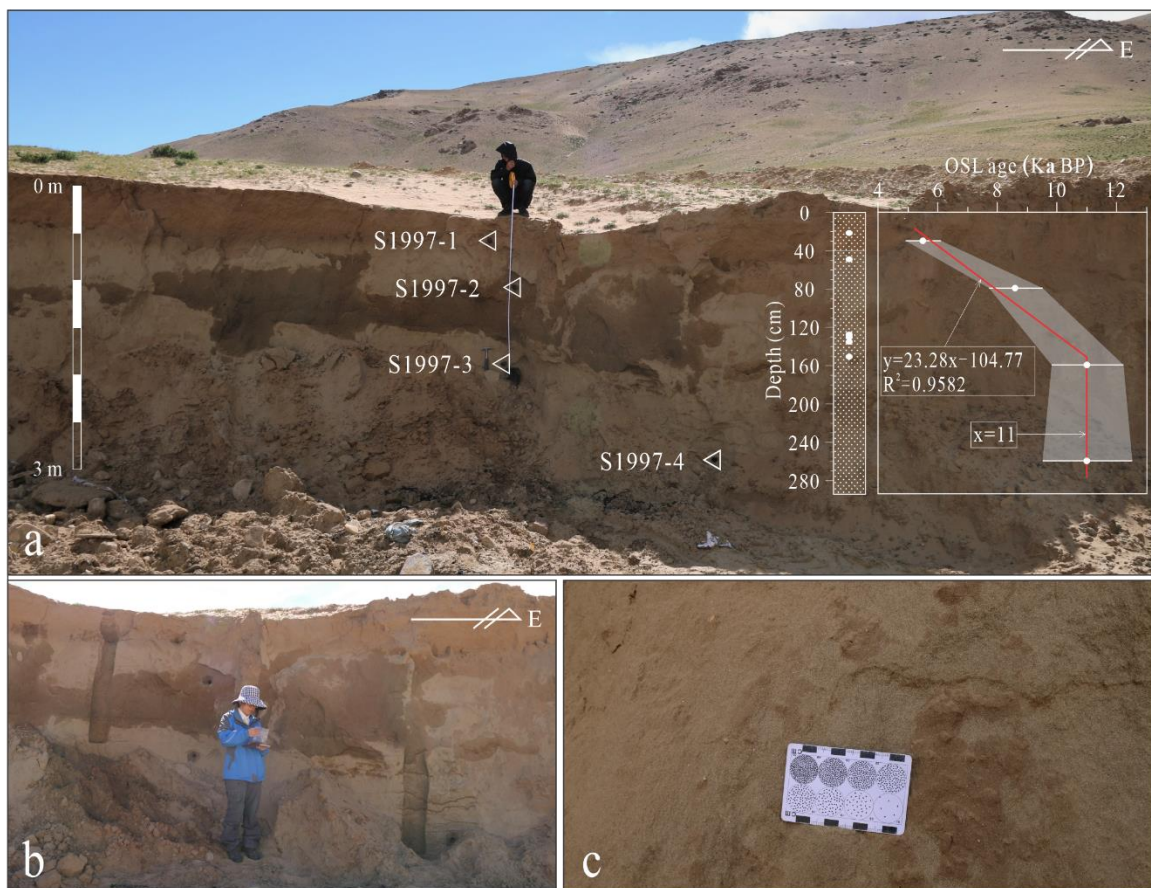
570

Figure 2: Photos of Profile Pala and sampling.

(**a**) Location and lithology of Profile Pala (about 300 cm in length, 28°18′57″ N, 87°25′26″ E, 4325 m.). Triangles indicate four OSL dating samples which were drilled from the depth of 30 cm, 80 cm, 160 cm, and 260 cm. The age-depth model for Profile Pala is built on the right side. (**b**) Sampling of paleoclimate samples. (**c**) Close-up photo of aeolian sediments.

575
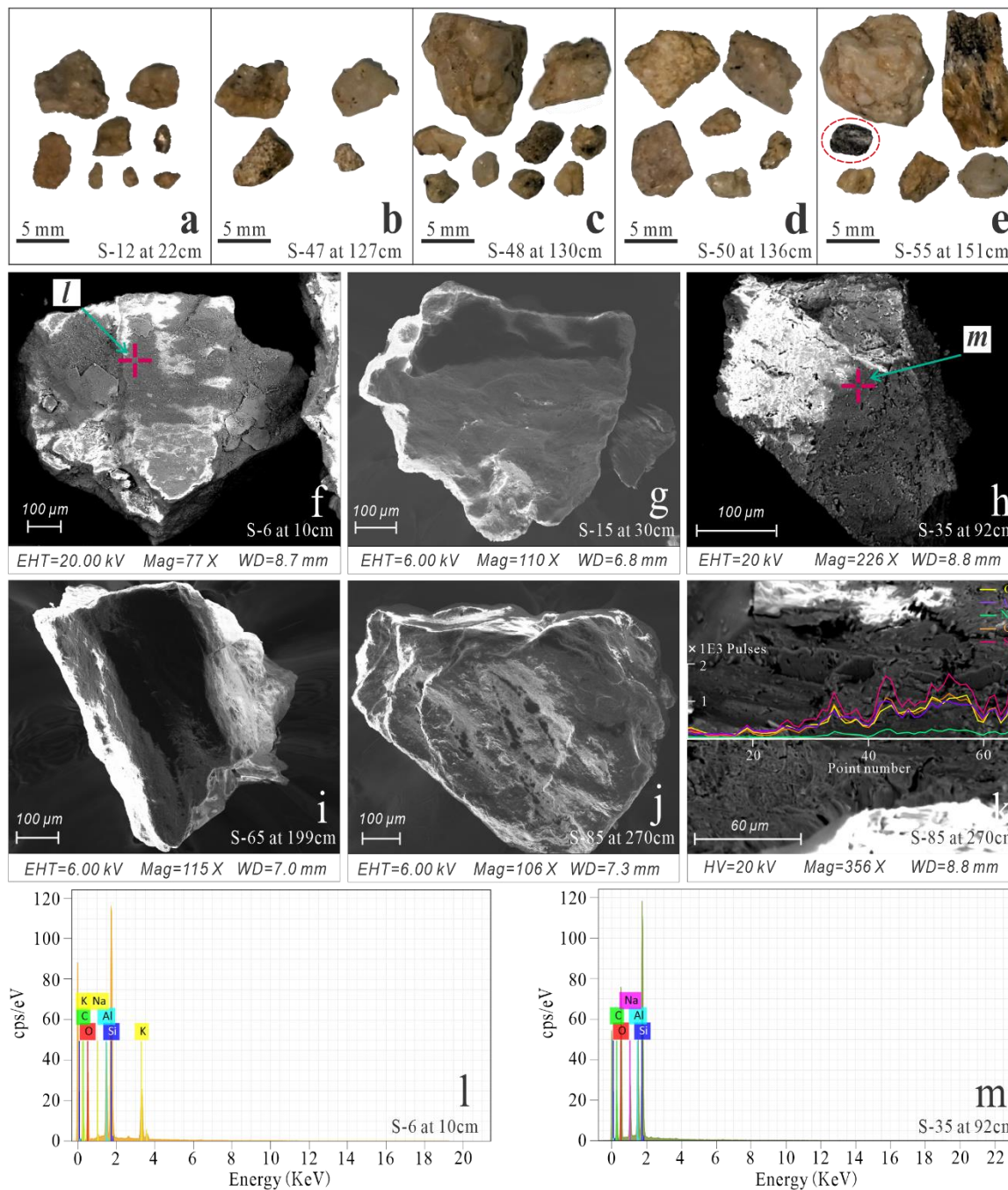
Figure 3: (a) - (c) Gravels scattered over the sands at the depth of 22 cm, 127 cm, 130 cm 136 cm, and 151 cm. **(f) - (k)** SEM photographs of representative samples at the different depths. In addition, the EDS spectrums of the white line are shown in the **f**. **(l) – (m)** EDS spectrums (taken at the labeled spots (red cross marks) from **f** and **h** at different depths.
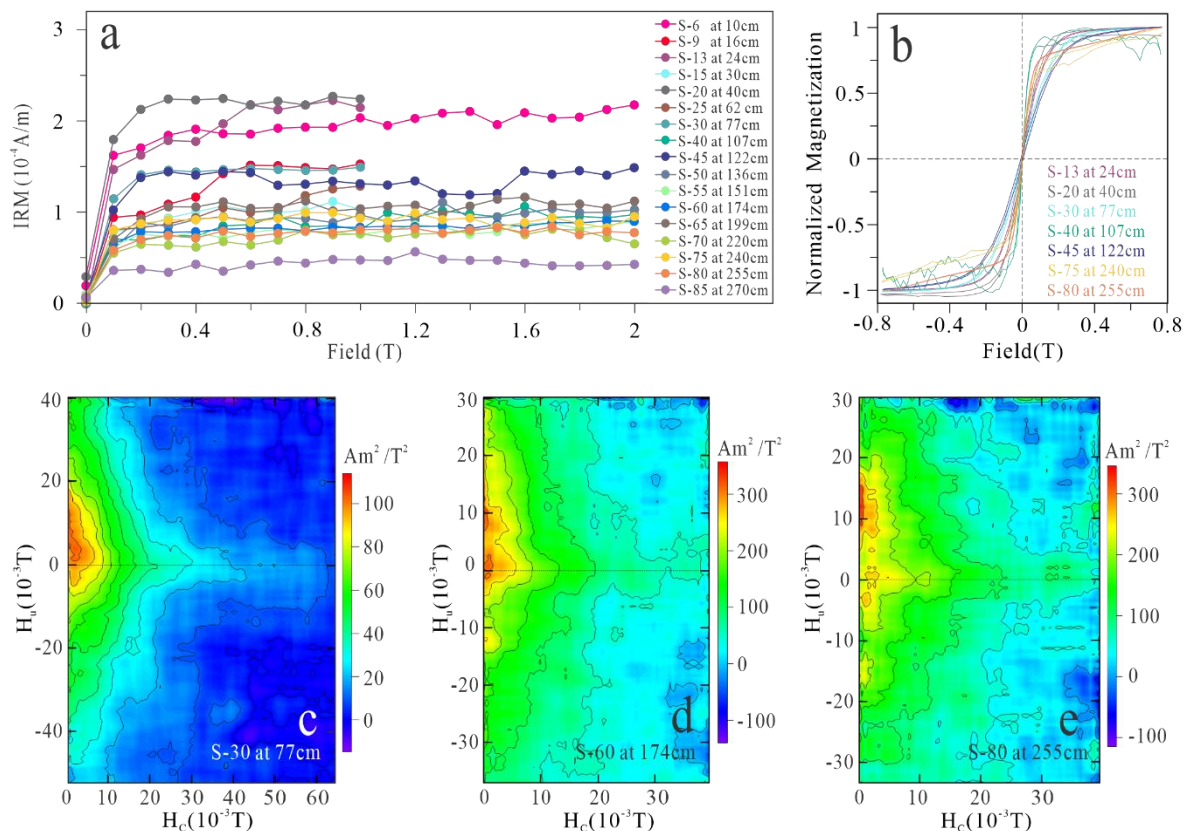
Figure 4: (a) Isothermal remanent magnetization (IRM) acquisition curves of typical samples at the different depths. **(b)** Hysteresis of typical samples at the different depths. **(c) - (e)** The first-order reversal curve (FORC) diagrams of typical samples under smoothing factors (SF) of 9, 10, 10 respectively.
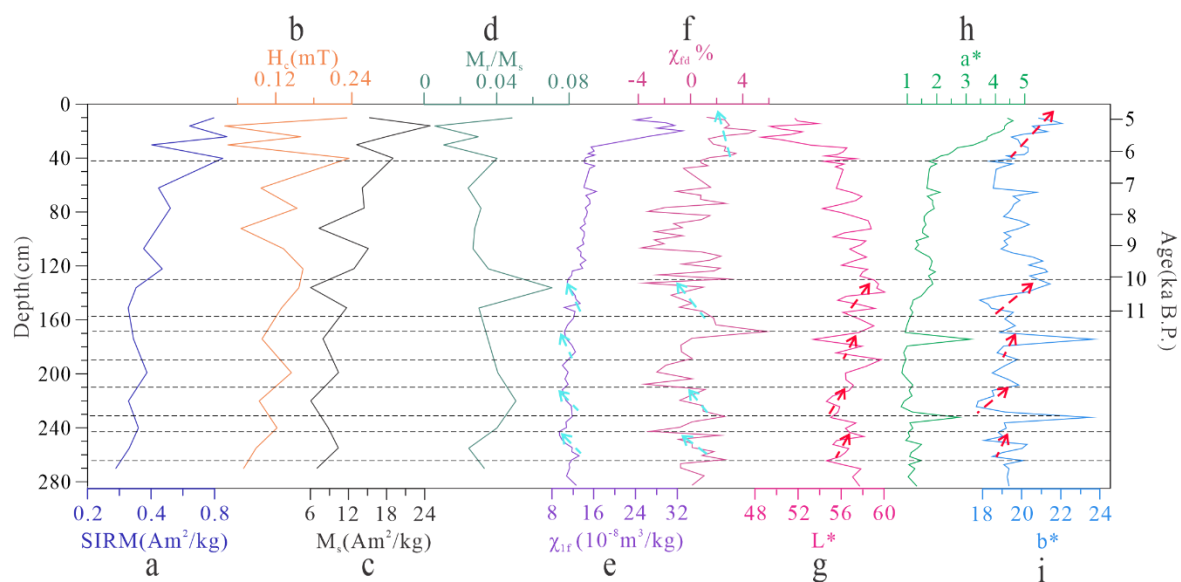
Figure 5: (a) - (d) Rock magnetism parameters. **(e)** Low-frequency magnetic susceptibility (χ_{lf}). **(f)** Frequency-dependent susceptibility ($\chi_{fd}\%$). **(g) - (i)** Color variations.
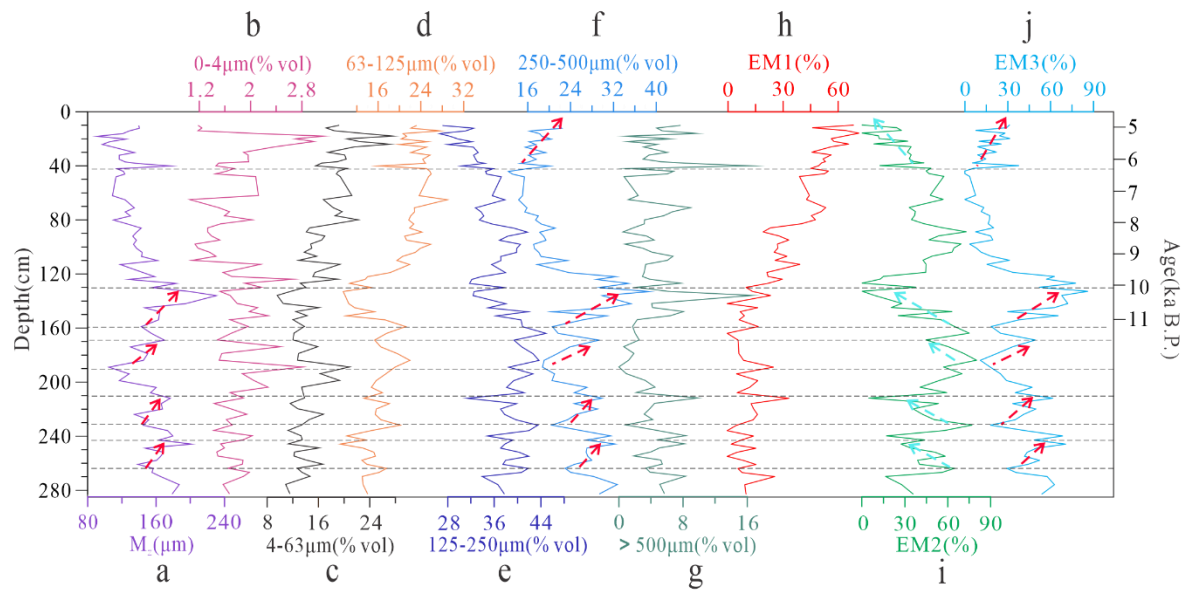
Figure 6: (a) - (g) Grain size parameters. **(h) - (j)** The end member (EM) analysis results of the grain size distribution (GSD) at the different depths.
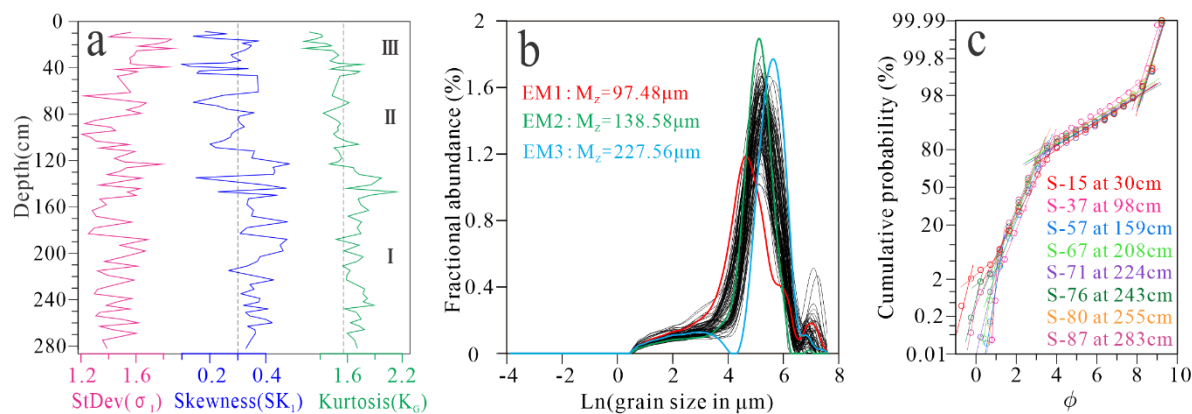
Figure 7: **(a)** Standard deviation, skewness, and kurtosis. **(b)** Frequency curves and end member (EM) analysis results of the grain size distribution (GSD). **(c)** Probability cumulative curves of representative samples at the different depths.
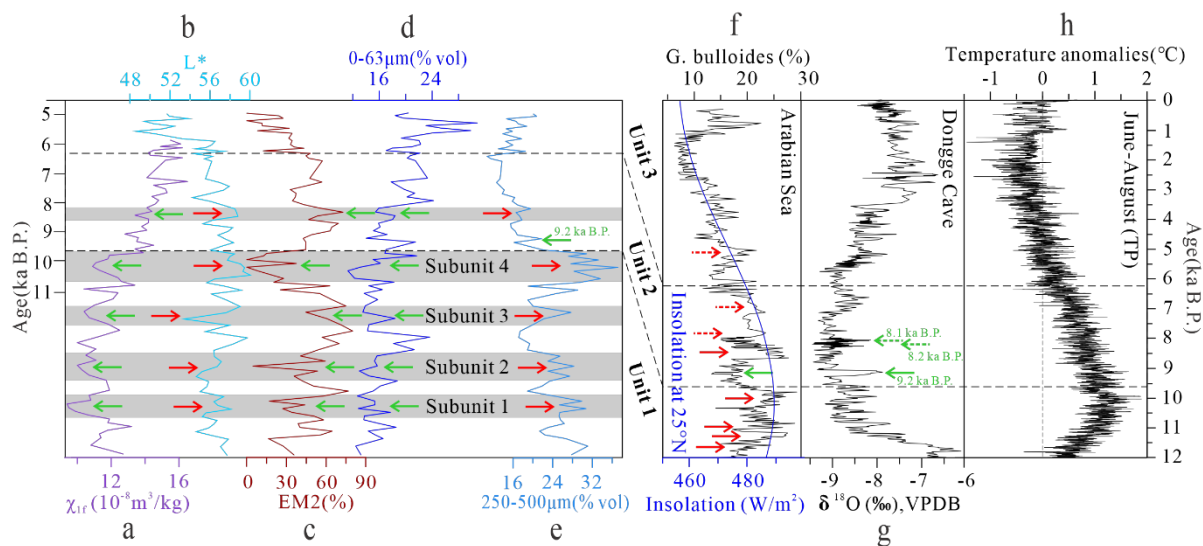
Figure 8: Comparison of the low-frequency magnetic susceptibility (χ_{lf}) (**a**) with the percentage of frequency-dependent susceptibility ($\chi fd\ \%$) (**b**), lightness (a^*) (**c**), the content of 0-63 μm (**d**) and 250-500 μm grains (**e**) the planktic foraminifera Globigerina bulloides (%) abundance (G. bulloides) (**f**) (Gupta et al., 2005; Gupta et al., 2013; Das et al., 2017) and summer insolation at 25° N (Dykoski et al., 2005), $\delta^{18}O$ (g) (Dykoski et al., 2005), and temperature anomalies of Tibetan Plateau with respect to 1961-1990 CE (**h**).